ELECTRONIC RESEARCH ARCHIVE
Volume **28**, Number **2**, June **2020**
doi:10.3934/era.2020051
pp. **961–976**

AN ADAPTIVE EDGE FINITE ELEMENT METHOD FOR THE MAXWELL'S EQUATIONS IN METAMATERIALS

Hao Wang and Wei Yang

Hunan Key Laboratory for Computation and Simulation in Science and Engineering
School of Mathematics and Computational Science, Xiangtan University
Xiangtan 411105, Hunan, China

Yunqing Huang

Key Laboratory of Intelligent Computing & Information Processing of Ministry of Education
School of Mathematics and Computational Science, Xiangtan University
Xiangtan 411105, Hunan, China

Abstract. In this paper, we study an adaptive edge finite element method for time-harmonic Maxwell's equations in metamaterials. *A-posteriori* error estimators based on the recovery type and residual type are proposed, respectively. Based on our *a-posteriori* error estimators, the adaptive edge finite element method is designed and applied to simulate the backward wave propagation, electromagnetic splitter, rotator, concentrator and cloak devices. Numerical examples are presented to illustrate the reliability and efficiency of the proposed *a-posteriori* error estimations for the adaptive method.

1. **Introduction.** In this paper, we consider the following two-dimensional time harmonic Maxwell's equations

$$\nabla \times \left(\frac{1}{\mu}\nabla \times \boldsymbol{E}\right) - k^2\varepsilon \boldsymbol{E} = \boldsymbol{F}, \quad \text{in } \Omega, \tag{1}$$

where $\Omega \subset \mathbb{R}^2$ is a bounded domain with Lipschitz boundary $\partial\Omega$, $\boldsymbol{E} = [E_1, E_2]^t$ denotes electric field and $\boldsymbol{F} = [F_1, F_2]^t \in [L_2(\Omega)]^2$ represents the given wave source term, where $[L_2(\Omega)]^2$ is denoted as the two-dimensional vector space of square integrable functions. The parameters μ and ε are the permeability and permittivity of the material medium, which may be functions of position. And k is the wavenumber. The curl $\nabla\times$ of $v = [v_i]_{i=1}^d$ is defined differently depending on the space dimension d. For $d = 1$, the curl of a scalar v is defined as the vector $\nabla \times v = [\partial_y v_1, -\partial_x v_1]$. For $d = 2$, it is the number $\nabla \times v = \partial_x v_2 - \partial_y v_1$.

Solutions of many problems of interest require computation of phenomena occurring in a physical domain of infinite extent. In such an infinite domain, electromagnetic sources are all considered to be at the origin, and to scatter energy to infinity. A condition is required to prevent the nonphysical inverse process, where energy is transferred by radiation from infinity to the origin, and ensure uniqueness

2020 *Mathematics Subject Classification.* 78M10, 65N30.
Key words and phrases. Maxwell's equations, wave source terms, *a-posteriori* error estimator, adaptive edge finite element method, metamaterial media.

of the solution in an infinite domain. For the two-dimensional case, the following condition, known as the Silver-Müller radiation condition [5], must be satisfied

$$\lim_{r\to\infty} r^{1/2}\left(\nabla\times\boldsymbol{E}\times\boldsymbol{n}-ik\boldsymbol{E}\right)=0,\quad r=|x|. \tag{2}$$

The numerical approximations of the Maxwell's equations have been extensively investigated in the last many years, such as finite element method (FEM) [6, 7, 15, 18, 23, 36], finite difference time domain method (FDTD) [14, 30], interior penalty discontinuous Galerkin method (IPDG) [17], hybridizable discontinuous Galerkin method (HDG) [27], nodal discontinuous Galerkin method (NDG) [22] and multigrid method (MG) [11], etc. In recent years, metamaterials as a new type of material have attracted people's attention because of their potential applications in many fields [14, 28], such as cloaking devices [2, 12, 24], sub-wavelength imaging and perfect lens. We mention in passing some related mathematical research on metamaterials in the literature [1, 4, 20, 21], and some related finite element methods designed for simulating the electromagnetic wave in metamaterlals [33, 34, 35]. The advantage of adaptive finite element method in metamaterials, which will be considered in this paper, is to make possible, with reasonable computational cost, the local mesh adjustment of the computational domain according to *a-posteriori* error estimator.

The adaptive method can improve the efficiency of electromagnetic field calculation, and it is simple and and accurate [6, 7, 23]. In this paper, we develop the adaptive finite element method of Maxwell's equation in metamaterials. Because many electromagnetic problems are actually interface problems, we need to deal with them carefully. Some parts of the interface problems do not need to be refined near the interface, but they are still refined by using the usual indicators. So the more efficient *a-posteriori* error estimator should be considered without regard to the particularity of the examples and make the meshes match the images of the numerical solution better, which is the purpose of this article. In view of such problems, the recovery technique is used in each sub-area and the corresponding error is calculated. Errors of all sub-areas constitute errors of the domain of interest to guide the grid refinement.

The rest of this paper is organized as follows. In Section 2, we introduce the finite element scheme for the Maxwell's equations. *A-posteriori* error estimators are proposed, which include two types: one is the residual-based and the other is the recovery-based in Section 3. Afterwards in Section 4, several numerical examples are presented to compare the realization effect of the different *posteriori* error indicators. In Section 5, we give a conclusion.

2. **Finite element scheme.**

Let $L_2(\Omega)$ be the Hilbert space of square integrable functions on Ω equipped with the standard L_2-norm: $\|w\|=\sqrt{(w,w)}$, where $(\cdot,\cdot)$ is standard L_2-inner product. Consider the following Hilbert space

$$H(\mathrm{curl};\Omega)=\left\{\boldsymbol{v}=[v_1,v_2]^t\in[L_2(\Omega)]^2:\nabla\times\boldsymbol{v}\in L_2(\Omega)\right\},$$

and the subspace

$$H_0(\mathrm{curl};\Omega)=\left\{\boldsymbol{v}\in H(\mathrm{curl};\Omega):\boldsymbol{n}\times\boldsymbol{v}=n_1v_2-n_2v_1=0 \text{ on } \partial\Omega\right\},$$

equipped with the norm

$$\|\boldsymbol{v}\|_{H(\mathrm{curl};\Omega)}=\left(\|\nabla\times\boldsymbol{v}\|^2+\|\boldsymbol{v}\|^2\right)^{\frac{1}{2}},$$

where $\boldsymbol{n}$ is the unit outward normal vector to $\partial\Omega$.

The Berenger PML [3] is applied to approximate the Silver-Müller radiation condition with the perfect electric conductor (PEC) boundary conditions

$$\boldsymbol{n} \times \boldsymbol{E} = 0, \quad \text{on } \partial\Omega. \tag{3}$$

The variational formulation of Eq.(1) reads: Given $\boldsymbol{F} \in [L_2(\Omega)]^2$, find $\boldsymbol{E} \in H_0(\text{curl}; \Omega)$ such that

$$a(\boldsymbol{E}, \Psi) = (\boldsymbol{F}, \Psi), \quad \forall\ \Psi \in H_0(\text{curl}; \Omega), \tag{4}$$

where

$$a(\boldsymbol{E}, \Psi) = (\mu^{-1}\nabla \times \boldsymbol{E}, \nabla \times \Psi) - k^2(\varepsilon \boldsymbol{E}, \Psi).$$

Let $\mathcal{T}_h = \{K\}$ be a regular triangle partition of the domain Ω with mesh size h, define the lowest order edge elements space [25]

$$\boldsymbol{V}_h = \left\{ \Psi_h \in H(\text{curl}; \Omega) : \Psi_h\big|_K = \begin{bmatrix} a_1 \\ a_2 \end{bmatrix} + b \begin{bmatrix} y \\ -x \end{bmatrix},\ a_1, a_2, b \in R,\ \forall K \in \mathcal{T}_h \right\}.$$

A basis for $\boldsymbol{V}_h$ is given by the set of Nédélec's shape functions $\{\phi_i\}_{i=1}^{n_e}$ with n_e the number of triangle edges in the mesh, the simple formula for local shape functions is defined as

$$\phi_E^K = \lambda_i \nabla \lambda_j - \lambda_j \nabla \lambda_i \tag{5}$$

for any triangle $K \in \mathcal{T}_h$, $E = [v_i, v_j] \subset \overline{K}$ with vertices $\{v_i = (x^i, y^i)\}_{i=1}^3$, and associated with linear Lagrangian basis functions $\{\lambda_i\}_{i=1}^3$, where the explicit expressions for the basis λ_i of the triangle K is given by

$$\lambda_i = \frac{x^j y^k - x^k y^j}{2|K|} + \frac{y^j - y^k}{2|K|} x + \frac{x^k - x^j}{2|K|} y,$$

with cyclic permutation of the indices $\{i, j, k\}$ over $\{1, 2, 3\}$ and $|K|$ is the area of K. It can be shown that edge finite elements guarantee the continuity of the tangential component across faces shared by adjacent triangles; they thus fit the continuity properties of the electric field.

With the choice of discrete space $\boldsymbol{V}_h$, the curl-conforming finite element scheme of Eq.(4) takes the form as follows: Given $\boldsymbol{F} \in [L_2(\Omega)]^2$, seek $\boldsymbol{E}_h \in \boldsymbol{V}_h$ such that

$$a(\boldsymbol{E}_h, \Psi_h) = (\boldsymbol{F}, \Psi_h), \quad \forall\ \Psi_h \in \boldsymbol{V}_h. \tag{6}$$

3. *A-posteriori* error estimations.

Having computed a finite element solution, it is possible to obtain *a-posteriori* error estimations. These estimations accomplish two main goals. Firstly, they are able to quantify the actual error numerically. Secondly, they can be used to perform the *adaptive mesh refinement*, which solves the problem iteratively. The method uses *a-posteriori* error estimators to indicate where errors are particularly high, and more mesh intervals are then placed in those locations. This process

$$\text{Solve} \implies \text{Estimate} \implies \text{Mark} \implies \text{Refine}$$

can be repeated until a satisfactory error tolerance or result is reached. In this section, we propose *a-posteriori* error estimations including not only a residual type but also a recovery type. A Dörfler marking strategy [13] is used in the adaptive process.

3.1. **The residual-based *a-posteriori* error estimation.** The residual type *a-posteriori* error estimator $\eta_{K_l}^{r0}$ [15] for the element K_l is defined as

$$\eta_{K_l}^{r0} = \left(h_{K_l}^2 \left(\|R_{K_l}^1\|^2 + \|R_{K_l}^2\|^2 \right) + \sum_{E \in \mathcal{E}} h_{K_l} \left(\|J_E^1\|^2 + \|J_E^2\|^2 \right) \right)^{\frac{1}{2}}, \quad K_l \in \mathcal{T}_h, \quad (7)$$

where $\mathcal{E}$ denotes the set of all interior edges, $h_{K_l} = |K_l|^{1/2}$ is the the diameter of K_l, and the local contributions $R_{K_l}^1, R_{K_l}^2$ and J_E^1, J_E^2 are defined, respectively, as

$$R_{K_l}^1 = \nabla \times \left(\mu^{-1} \nabla \times \boldsymbol{E} \right) - k^2 \varepsilon \boldsymbol{E} - \boldsymbol{F},$$
$$R_{K_l}^2 = \nabla \cdot \left(k^2 \varepsilon \boldsymbol{E} + \boldsymbol{F} \right),$$

and

$$J_E^1 = \left[\left(\mu^{-1} \nabla \times \boldsymbol{E} \right) \cdot (n_{E_2}, -n_{E_1})^t \right]_E,$$
$$J_E^2 = \left[\left(k^2 \varepsilon \boldsymbol{E} + \boldsymbol{F} \right) \cdot (n_{E_1}, n_{E_2})^t \right]_E,$$

where $[\boldsymbol{F} \cdot \boldsymbol{v}]_E := \boldsymbol{F} \cdot \boldsymbol{v}|_{K_m} - \boldsymbol{F} \cdot \boldsymbol{v}|_{K_n}$ on the edge E for $E = K_m \cap K_n$, $K_m, K_n \in \mathcal{T}_h$.

3.2. **The recovery-based *a-posteriori* error estimations.** The recovery type *a-posteriori* error estimators $\eta_{K_l}^{r1}$ [23] and $\eta_{K_l}^{r2}$ are considered, respectively, as

$$\eta_{K_l}^{r1} = \left(\|R(\nabla \times \boldsymbol{E}) - \nabla \times \boldsymbol{E}\|^2 + \|R(\boldsymbol{E}) - \boldsymbol{E}\|^2 \right)^{\frac{1}{2}}, \quad (8)$$

and

$$\eta_{K_l}^{r2} = \left(\|R(\mu^{-1} \nabla \times \boldsymbol{E}) - \mu^{-1} \nabla \times \boldsymbol{E}\|^2 + \|R(\varepsilon \boldsymbol{E}) - \varepsilon \boldsymbol{E}\|^2 \right)^{\frac{1}{2}}, \quad (9)$$

for $K_l \in \mathcal{T}_h$, here R denotes the recovery operator. The specific recovery algorithm see the Algorithm 1.

Algorithm 1

- For the interior edge $\boldsymbol{E}_i$, we select two elements K_{i1}, K_{i2} sharing it, i.e., $\boldsymbol{E}_i = K_{i1} \cap K_{i2}$. At the midpoint $\boldsymbol{x}_i$ of the edge $\boldsymbol{E}_i$, we take

  $$R\left(\alpha_i \nabla \times \boldsymbol{E}(\boldsymbol{x}_i)\right) = \frac{1}{2} \left(\alpha_i \nabla \times \boldsymbol{E}(\boldsymbol{x}_i)|_{K_{i1}} + \alpha_i \nabla \times \boldsymbol{E}(\boldsymbol{x}_i)|_{K_{i2}} \right),$$

  and

  $$R\left(\beta_i \boldsymbol{E}(\boldsymbol{x}_i)\right) = \frac{1}{2} \left(\beta_i \boldsymbol{E}(\boldsymbol{x}_i)|_{K_{i1}} + \beta_i \boldsymbol{E}(\boldsymbol{x}_i)|_{K_{i2}} \right),$$

  where $i = 1, 2$. Take $\alpha_1 = 1$, $\beta_1 = 1$ for Eq.(8) and $\alpha_2 = \mu^{-1}$, $\beta_2 = \varepsilon$ for Eq.(9), respectively.
- For the boundary edge $\boldsymbol{E}_i$, we find several interior edges that are closer to it and by linear interpolation, we can obtain $R(\alpha_i \nabla \times \boldsymbol{E})$ and $R(\beta_i \boldsymbol{E})$ at the midpoint $\boldsymbol{x}_i$ of the edge $\boldsymbol{E}_i$.

Remark 1. Recovery operator can be built in a variety of ways such as gradient recovery [19, 26, 37], functional recovery [29], flux recovery [8, 9, 10, 31] and so on. Two quantities related to $\mu^{-1} \nabla \times \boldsymbol{E}$ and $\varepsilon \boldsymbol{E}$ are recovered in the respective H(curl)-and H(Div)-conforming finite element spaces in [9, 10]. It is different that we take average of flux to construct the flux recovery operator, which is easy to implement with superconvergence.

Theorem 3.1. *Assume that the domain Ω is covered by a triangular mesh formed by parallelograms, and under the assumption* [23, Lemma 2.6]*:*
(1) Assume that $|\mu^{-1}| < C_1$, for any function $\boldsymbol{u} = (u_1, u_2)^T \in (W^{3,\infty}(\Omega))^2$ and any parallelogram center $\boldsymbol{x}_e$, we have

$$\left|\mu^{-1}(\boldsymbol{x}_e)\nabla \times \boldsymbol{u}(\boldsymbol{x}_e) - R\left(\mu^{-1}(\boldsymbol{x}_e)\nabla \times \boldsymbol{u}_I(\boldsymbol{x}_e)\right)\right| \le Ch^2. \tag{10}$$

(2) Assume that $|\varepsilon_i| < C_2 (i = 1, 2, 3, 4)$ with $\varepsilon = [\varepsilon_1, \varepsilon_2; \varepsilon_3, \varepsilon_4]$, for $\boldsymbol{E} \in (W^{2,\infty}(\Omega))^2$ and h is enough small with any parallelogram center $\boldsymbol{x}_e$, we have

$$|\varepsilon(\boldsymbol{x}_e)\boldsymbol{E}(\boldsymbol{x}_e) - R(\varepsilon(\boldsymbol{x}_e)\boldsymbol{E}_I(\boldsymbol{x}_e))| \le Ch^2. \tag{11}$$

(3) Under the assumption of (1) and (2) above, $\boldsymbol{E}$ and $\boldsymbol{E}_h$ satisfy Eqs.(4) and (6), respectively. If $\boldsymbol{E} \in (W^{3,\infty}(\Omega))^2$ and h is enough small, then we have

$$\left\|\mu\boldsymbol{E} - R\left(\mu^{-1}\boldsymbol{E}_h\right)\right\|_{l_2,\Omega} + \|\varepsilon\nabla \times \boldsymbol{E} - R(\varepsilon\nabla \times \boldsymbol{E}_h)\|_{l_2,\Omega} \le Ch^2. \tag{12}$$

Remark 2. The proof of Theorem 3.1 is similar to the reference of [23, Lemma 2.7], [16, Theorem 3.3] and [23, Theorem 2.2].

4. **Numerical examples.** This section is devoted to numerical examples to illustrate the efficiency and reliability of the proposed *a-posteriori* error indicators. The wave source term is given by $\boldsymbol{F} = k^2\boldsymbol{P}\exp(ik\boldsymbol{d}\cdot\boldsymbol{x})q(\boldsymbol{x})$, where $i = \sqrt{-1}$ is the imaginary unit. For simplicity, we use the Ndof and I to denote the number of degrees of freedom and the identity matrix, respectively.

Example 4.1. Let $\Omega = [-1, 1] \times [-1, 1]$ and take the coefficients as follows

$$k = 1, \quad \mu = \frac{1}{1 + x^2 + y^2}, \quad \epsilon = \begin{bmatrix} 1 + x^2 & xy \\ xy & 1 + y^2 \end{bmatrix}.$$

We choose the analytic solution

$$\boldsymbol{E} = \begin{bmatrix} \dfrac{y(x^2-1)(y^2-1)}{x^2+y^2+0.02} \\ \dfrac{-x(x^2-1)(y^2-1)}{x^2+y^2+0.02} \end{bmatrix},$$

and compute $\boldsymbol{F}$ accordingly.

The Example 4.1 is aimed to test the convergence result stated in Theorem 3.1. Clearly, the results shown in Table 1 are consistent with Theorem 3.1.

h	$\|R(\mu^{-1}\nabla \times \boldsymbol{E}) - \mu^{-1}\nabla \times \boldsymbol{E}\|_{l_2}$	Rate	$\|R(\varepsilon\boldsymbol{E}) - \varepsilon\boldsymbol{E}\|_{l_2}$	Rate
1/2	1.72241533259	$*$	0.65798419344	$*$
1/4	1.43147288047	0.2669	0.33590028941	0.9700
1/8	1.04238857427	0.4576	0.09973181632	1.7519
1/16	0.33780141151	1.6256	0.02622591011	1.9271
1/32	0.08957072297	1.9151	0.00685496133	1.9358
1/64	0.02277727214	1.9754	0.00173714021	1.9804

TABLE 1. The Discrete l_2 errors and convergence rate.

Example 4.2. Let Ω be the rectangular domain $[-2, 2] \times [-5, 2]$, the parameters μ and ε are taken, respectively, as

$$\mu = \begin{cases} -1.1, & \Omega_1, \\ 1, & \Omega\backslash\Omega_1, \end{cases}$$

and

$$\varepsilon = \begin{cases} -1.1I, & \Omega_1, \\ I, & \Omega\backslash\Omega_1, \end{cases}$$

where the negative index metamaterial medium area $\Omega_1 = [-2,2] \times [-2.5,-0.5]$. We choose $k = 10, \boldsymbol{P} = [1,0]^t, \boldsymbol{d} = [0,1]^t$ and $q(\boldsymbol{x}) = 1 - 4(x^2 + (y-1.45)^2)$ in the ball with a center $(0, 1.45)$ of radius $1/2$ and $q(\boldsymbol{x}) = 0$ outside. In our simulation, we choose a uniform mesh with $h = 0.1$ and use a PML with 5 cells in thickness around the rectangular domain.

Example 4.2 simulates the backward wave propagation phenomenon illustrated in Fig.1, which is based on the three types *a-posteriori* error indicators mentioned above. It can see that wave propagates as usual before it enters the metamaterial region. Once the wave enters into the metamaterial, wave propagates backward inside the metamaterial slab. And that wave propagates as usual again when leaves the metamaterial slab.

From the point of view of suitability between the grid and the numerical solution, it can be seen that the residual type is better than the others in Fig.1. From the numerical solution of the images, some parts of the horizontal interfaces between the two media do not need to be refined, but in fact, these places are still refined when using the recovery *a-posteriori* error indicators.

Thus according to two horizontal interfaces formed between the media, we divide the whole area into three sub-areas, and the recovery type *a-posteriori* error of the whole area is consisted of these sub-areas, which are shown in Fig.2. Compared with the direct recovery type *a-posteriori* error of the whole area in Fig.1, adaptive meshes by using the recovery type *a-posteriori* error of the whole area consisted of the error for these sub-areas perform better on the interfaces during the refinement process, which achieves the expected effect.

Remark 3. In Example 4.3-4.6, we also first consider the three types a posteriori error indicators mentioned above on the whole area and then consider that according to the number of interfaces n formed between the media, the entire area can be divided into $n+1$ sub-areas, which each sub-area is independent and parallel computing can be considered, the recovery type a posteriori error of the whole area is consisted of the error for these sub-areas.

Example 4.3. Let $\Omega = [-2,2] \times [-3,2]$ be a rectangular domain with $k = 10, \boldsymbol{P} = [1,0]^t, \boldsymbol{d} = [0,1]^t$ and $q(\boldsymbol{x}) = \mathrm{erfc}(5((x-x_0)^2 + (y-y_0)^2 - 1))/2$, where $\mathrm{erfc}(x) = \frac{2}{\sqrt{\pi}} \int_x^\infty \exp(-t^2)dt$. The parameters μ and ε are defined as follows

$$\mu = 1, \quad \boldsymbol{x} \in \Omega,$$

and

$$\varepsilon(\cdot, y) = \begin{cases} \begin{bmatrix} 1+m_p^2 & m_p \\ * & 1 \end{bmatrix}, & y_1 \le y \le y_2, \\ I, & y < y_1 \text{ or } y > y_2, \end{cases}$$

which can be easily derived according to the theory of article [36] while the wave propagates along the y-axis. The constant m_p is called "moving parameter" and the symbol "$*$" denotes as the symmetric part of the matrix. In our simulation, we choose a uniform mesh with $h = 0.1$ and use a PML with 5 cells in thickness around the rectangular domain.

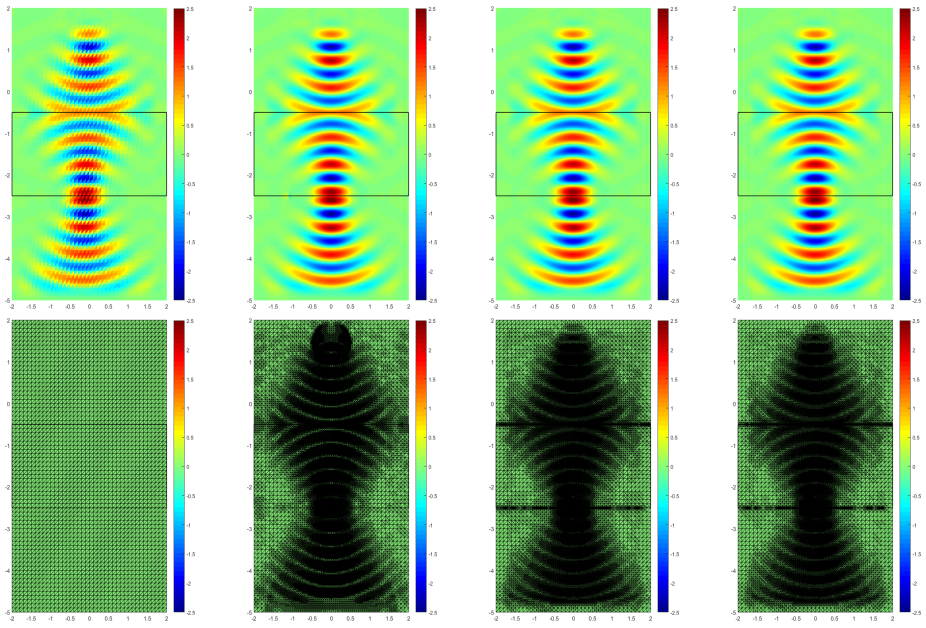

FIGURE 1. Example 4.2: The first line and the second line are the real values of E_1 and the meshes, respectively. From left to right: 8510 Ndof (for the initial mesh), 133620 Ndof (by using $\eta^{r0}_{K_l}$) after 14 refinements, 139743 Ndof (by using $\eta^{r1}_{K_l}$) and 132334 Ndof (by using $\eta^{r2}_{K_l}$) with the same times of 12 refinements.

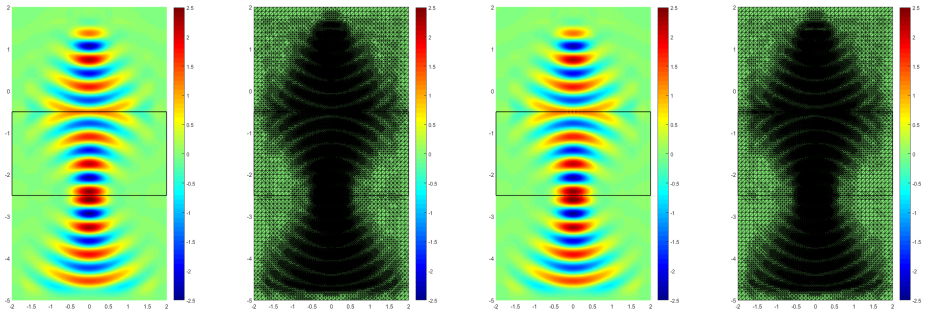

FIGURE 2. Example 4.2: Snapshots of numerical solution and adaptive meshes for the real values of E_1 after 10 refinements. First two columns: 142833 Ndof (by using $\eta^{r1}_{K_l}$); The last two columns: 138064 Ndof (by using $\eta^{r2}_{K_l}$).

In Example 4.3, the moving medium area is fixed in $\Omega_1 = [-2, 2]\times[-0.5, 0]$, which can be denoted as the union of $\Omega_2 = [-2, 0] \times [-0.5, 0]$ and $\Omega_3 = [0, 2] \times [-0.5, 0]$. We achieve the different moving effects by the different choices of the center point (x_0, y_0) and the parameter m_p.

Firstly, we choose the center point $(x_0, y_0) = (1, 1.45)$ with $m_p = 2$ for the domain Ω_1, i.e., the wave source is fixed in the upper right. Clearly, we can see that the

wave moves from right to left after wave passes the moving medium area shown in Figs.4 and 5.

Then, the center point $\boldsymbol{x}_0 = (x_0, y_0)$ are chosen as $(-1, 1.45)$ with $m_p = -2$ for the domain Ω_1, i.e., the wave source is fixed in the upper left. Obviously, we can see that the wave moves from left to right after wave passes the moving medium area shown in Figs.6 and 7.

Finally, the constant m_p is taken as 2 for domain Ω_2 and -2 for domain Ω_3 with the center point $\boldsymbol{x}_0 = (0, 1.45)$, i.e., the wave source is fixed in the upper middle. Evidently, we can see that the wave moves from the middle to left and right after wave passes the moving medium area shown in Figs.8 and 9.

Overall, it can be seen that the recovery type *a-posteriori* error indicators perform better.

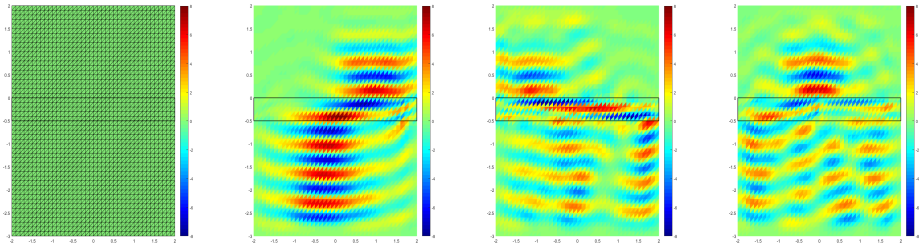

FIGURE 3. Example 4.3: The first is the initial mesh with 6090 Ndof and the last three are the real values of E_1 based on the initial mesh.

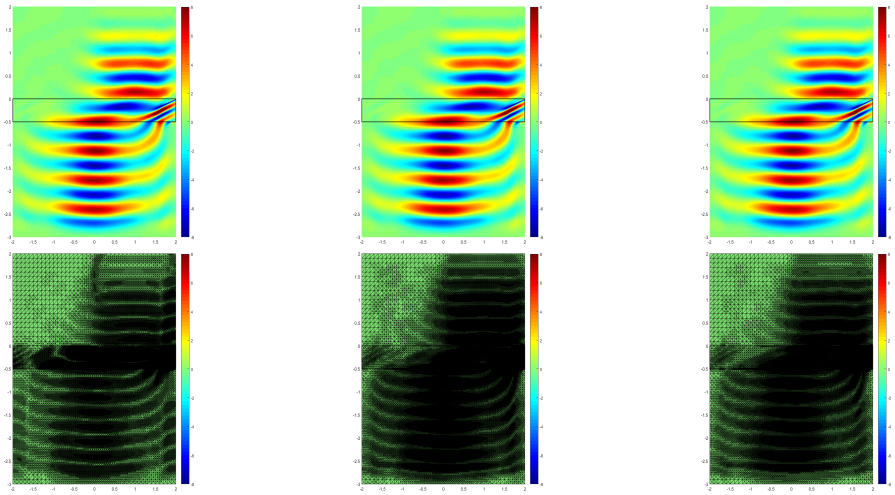

FIGURE 4. Example 4.3: The first line and the second line are the real values of E_1 and the meshes with $(x_0, y_0) = (1, 1.45)$ and $m_p = 2$, respectively. From left to right: 299395 Ndof (using $\eta_{K_l}^{r0}$) after 18 refinements, 315182 Ndof (by using $\eta_{K_l}^{r1}$) and 273473 Ndof (by using $\eta_{K_l}^{r2}$) with the same times of 13 refinements.

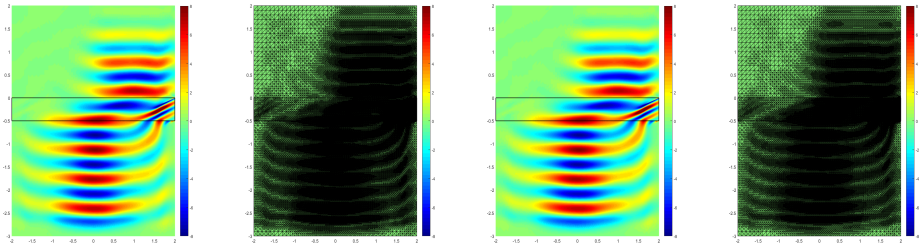

FIGURE 5. Example 4.3: Snapshots of numerical solution and adaptive meshes for the real values of E_1 after 13 refinements with $(x_0, y_0) = (1, 1.45)$ and $m_p = 2$. First two columns: 303142 Ndof (by using $\eta^{r1}_{K_l}$); The last two columns: 278572 Ndof (by using $\eta^{r2}_{K_l}$).

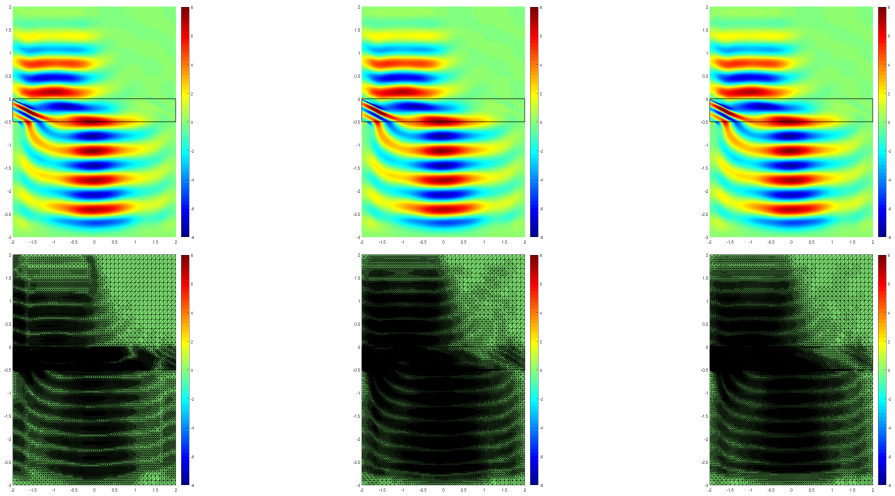

FIGURE 6. Example 4.3: The first line and the second line are the real values of E_1 and the meshes with $(x_0, y_0) = (-1, 1.45)$ and $m_p = -2$, respectively. From left to right: 265615 Ndof (by using $\eta^{r0}_{K_l}$) after 21 refinements, 282153 Ndof (by using $\eta^{r1}_{K_l}$) and 237085 Ndof (by using $\eta^{r2}_{K_l}$) with the same times of 14 refinements.

For Example 4.4-4.5, we consider the square domain $\Omega = [-1.5, 1.5] \times [-1.5, 1.5]$ with $k = 20, \boldsymbol{P} = [0, 1]^t, \boldsymbol{d} = [-1, 0]^t, q(\boldsymbol{x}) = 1$ and use a PML with 1/60 of the region in thickness.

Example 4.4. The parameters μ and ε are taken, respectively, as

$$\mu = 1, \quad \boldsymbol{x} \in \Omega,$$

and

$$\varepsilon = \begin{cases} \begin{bmatrix} \dfrac{r^2 + 2mxy + m^2y^2}{r^2} & \dfrac{-m(x^2 - y^2) - m^2xy}{r^2} \\ * & \dfrac{r^2 - 2mxy + m^2x^2}{r^2} \end{bmatrix}, & R_1 \le r \le R_2, \\ I, & \text{otherwise}, \end{cases}$$

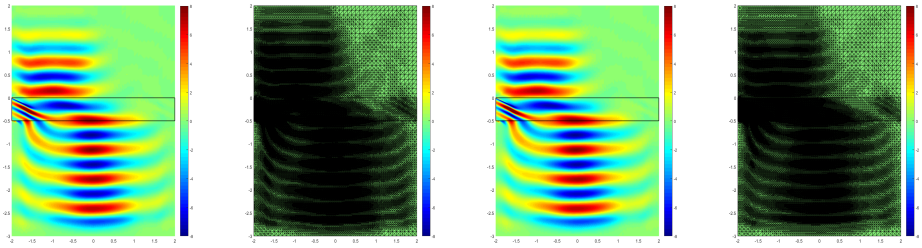

FIGURE 7. Example 4.3: Snapshots of numerical solution and adaptive meshes for the real values of E_1 after 14 refinements with $(x_0, y_0) = (-1, 1.45)$ and $m_p = -2$. First two columns: 282422 Ndof (by using $\eta_{K_l}^{r1}$); The last two columns: 245356 Ndof (by using $\eta_{K_l}^{r2}$).

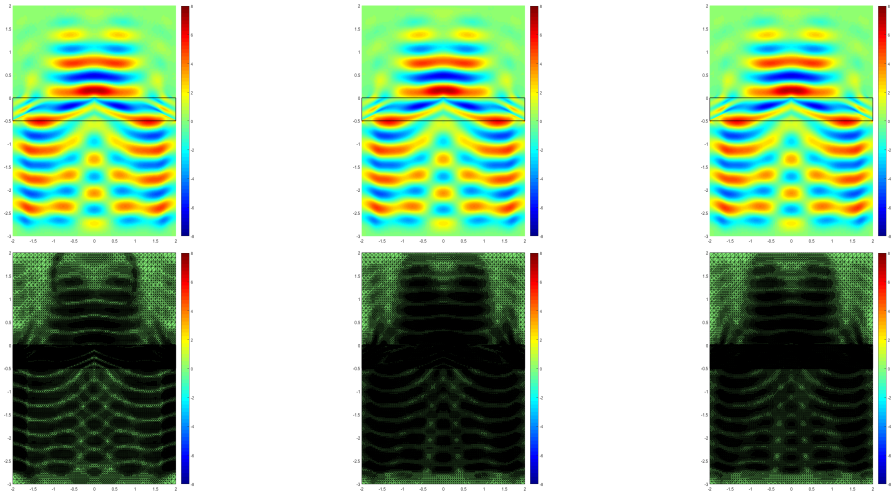

FIGURE 8. Example 4.3: The first line and the second line are the real values of E_1 and the meshes, respectively. From left to right: 323340 Ndof (by using $\eta_{K_l}^{r0}$) after 21 refinements, 306934 Ndof (by using $\eta_{K_l}^{r1}$) and 280265 Ndof (by using $\eta_{K_l}^{r2}$) with the same times of 13 refinements.

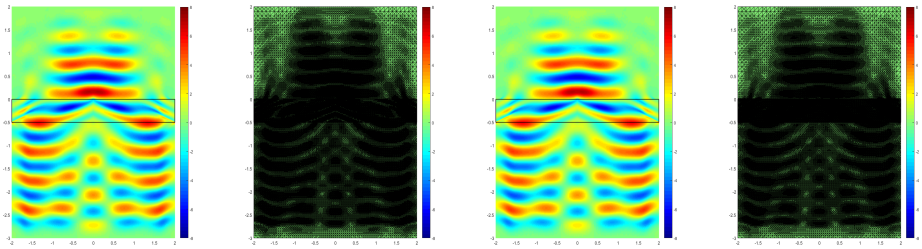

FIGURE 9. Example 4.3: Snapshots of numerical solution and adaptive meshes for the real values of E_1 after 13 refinements. First two columns: 284570 Ndof (by using $\eta_{K_l}^{r1}$); The last two columns: 271643 Ndof (by using $\eta_{K_l}^{r2}$).

where $m = \frac{\theta_0 r}{R_2 - R_1}$. Here, we choose the initial mesh with 167744 Ndof and take $R_1 = 0.2$, $R_2 = 2R_1$, $\theta_0 = \frac{\pi}{2}$ in the simulation.

In Example 4.4, we simulate the cylindrical rotation cloak. To see how wave propagates in the rotator, we plot the electric fields $\boldsymbol{E}$ in Figs.10 and 11. Clearly, it can be observed that the wave gets distorted in the metamaterial region and note that the parameter θ_0 determines the degree of distortion of the wave. Although the residual type *a-posteriori* error estimator achieves the rotation effect, the corresponding grid does not match the graphs of the numerical solution at all. In contrast, the recovery type *a-posteriori* error indicators are always good and meshes are more refined in the metamaterial region.

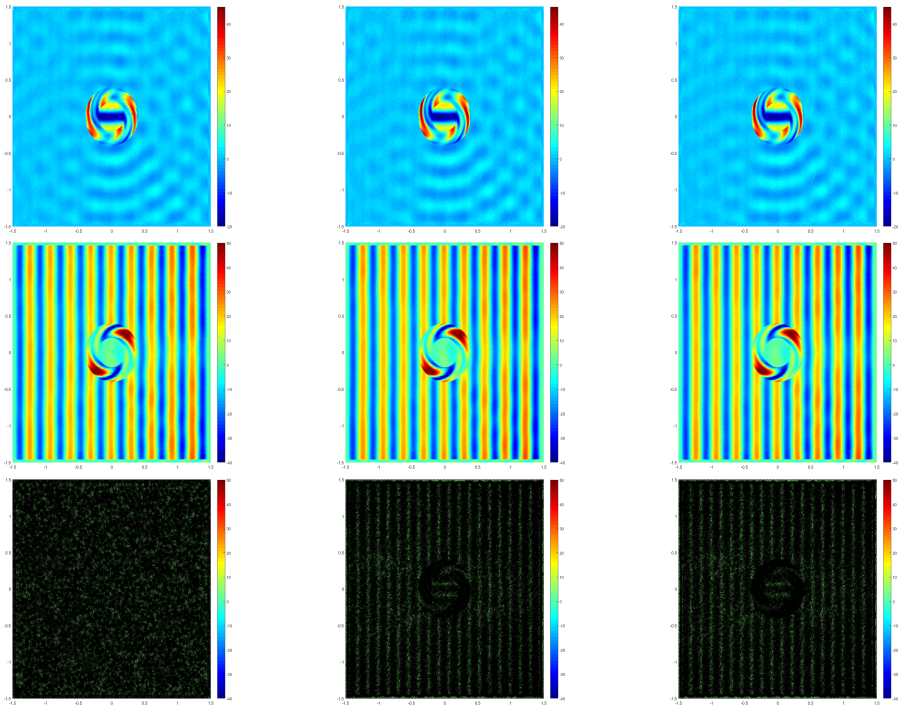

FIGURE 10. Example 4.4: The first line, the second line and the third line are the real values of E_1, the real values of E_2 and the meshes, respectively. From left to right: 344405 Ndof (by using $\eta_{K_l}^{r0}$) after 3 refinements, 344620 Ndof (by using $\eta_{K_l}^{r1}$) and 332141 Ndof (by using $\eta_{K_l}^{r2}$) with the same times of 17 refinements.

Example 4.5. We consider the parameters

$$\mu = \begin{cases} \dfrac{b^2}{a^2}, & 0 \le r \le a, \\ K_2 \varepsilon_r, & a \le r \le c, \\ 1, & \text{otherwise}, \end{cases}$$

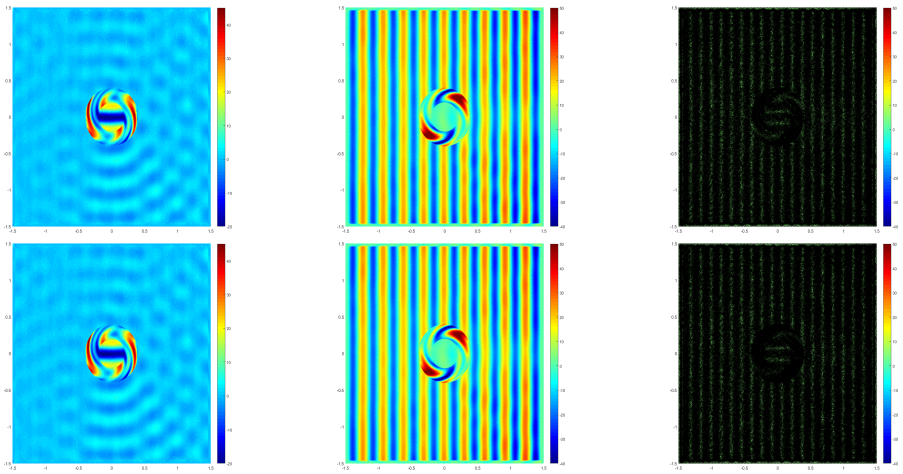

FIGURE 11. Example 4.4: The first column, the second column and the third column are snapshots of numerical solution for the real values of E_1, E_2 and adaptive meshes, respectively. The first line: 393423 Ndof after 23 refinements (by using $\eta_{K_l}^{r1}$); The second line: 416438 Ndof after 21 refinements (by using $\eta_{K_l}^{r2}$).

and

$$\varepsilon = \begin{cases} \begin{bmatrix} \varepsilon_r \cos^2\theta + \varepsilon_\theta \sin^2\theta & (\varepsilon_r - \varepsilon_\theta)\sin\theta\cos\theta \\ * & \varepsilon_r \sin^2\theta + \varepsilon_\theta \cos^2\theta \end{bmatrix}, & a \le r \le c, \\ I, & \text{otherwise}, \end{cases}$$

where the constants are denoted, respectively, as,

$$\varepsilon_r = \frac{r + K_1}{r}, \quad \varepsilon_\theta = \frac{1}{\varepsilon_r}, \quad K_1 = \frac{(b-a)}{c-b}c, \quad K_2 = \left(\frac{c-b}{c-a}\right)^2.$$

In our simulation, the parameters a, b and c are taken as 0.2, 0.4 and 0.6, respectively. There is 167744 Ndof in the initial mesh.

Example 4.5 simulates the electromagnetic concentration effect, which are shown in Figs.12 and 13. As in the previous example, although the residual type *a-posteriori* error estimator achieves the concentration effect, the pattern of the corresponding grid is not matched with the graph of the numerical solution. The advantage of recovery type *a-posteriori* errors is prominent again.

Example 4.6. Let Ω be the part of the square domain $[-1.5, 1.5] \times [-1.5, 1.5]$ outside the circle centered at origin with radius R_1. The computational areas Ω_1 and Ω_2 ($\Gamma = \Omega_1 \cap \Omega_2$) are shown in Fig.14. Here, we take $R_1 = 0.2$, $R_2 = 2R_1$ and the initial mesh with 20287 Ndof. We choose $k = 20, \boldsymbol{P} = [0, 1]^t, \boldsymbol{d} = [-1, 0]^t$ and $q(\boldsymbol{x}) = 1$. The parameters μ and ε are given as follows

$$\mu = \begin{cases} 1, & \boldsymbol{x} \in \Omega_1, \\ \left(\left(\frac{R_2 - R_1}{R_2}\right)^2 \frac{r}{r - R_1}\right)^{-1}, & \boldsymbol{x} \in \Omega_2, \end{cases}$$

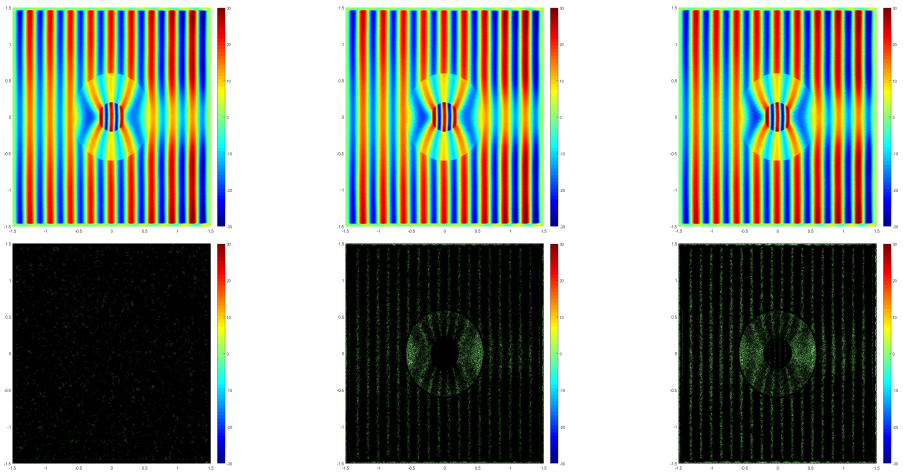

FIGURE 12. Example 4.5: The first line and the second line are the real values of E_2 and the meshes, respectively. From left to right: 794533 Ndof (by using $\eta_{K_l}^{r0}$) after 4 refinements, 506294 Ndof (by using $\eta_{K_l}^{r1}$) after 23 refinements and 505234 Ndof (by using $\eta_{K_l}^{r2}$) after 17 refinements.

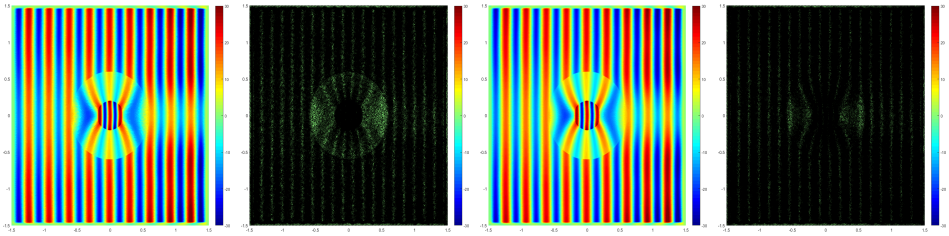

FIGURE 13. Example 4.5: Snapshots of numerical solution and adaptive meshes for the real values of E_2. First two columns: 468957 Ndof (by using $\eta_{K_l}^{r1}$) after 28 refinements; The last two columns: 656397 Ndof (by using $\eta_{K_l}^{r2}$) after 25 refinements.

and

$$\varepsilon = \begin{cases} I, & \boldsymbol{x} \in \Omega_1, \\ \begin{bmatrix} \dfrac{r^2 + R_1(R_1-2r)\cos^2\theta}{r(r-R_1)} & \dfrac{R_1(R_1-2r)\sin\theta\cos\theta}{r(r-R_1)} \\ * & \dfrac{r^2 + R_1(R_1-2r)\sin^2\theta}{r(r-R_1)} \end{bmatrix}, & \boldsymbol{x} \in \Omega_2. \end{cases}$$

In Example 4.6, the colaking simulation is displayed in Figs.15 and 16. It is obvious that the recovery-based *a-posteriori* error estimation $\eta_{K_l}^{r1}$ works well and the implementation is faster. Note that neither the permeability μ^{-1} nor the permittivity ε belongs to $L^\infty(\Omega)$, which is not under assumptions in Theorem 3.1. In spite of this, recovery-based *a-posteriori* error estimation $\eta_{K_l}^{r2}$ still works for this example.

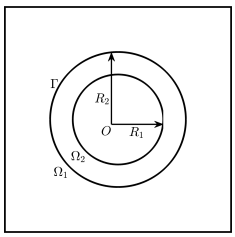

FIGURE 14. Example 4.6: The computational domain for the cloak simulation.

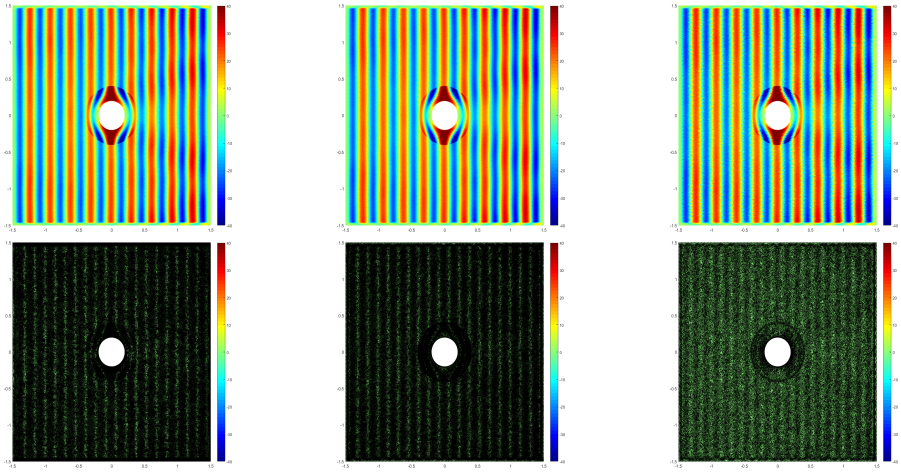

FIGURE 15. Example 4.6: The first line and the second line are the real values of E_2 and the meshes, respectively. From left to right: 445224 Ndof (by using $\eta_{K_l}^{r0}$) after 126 refinements, 323420 Ndof (by using $\eta_{K_l}^{r1}$) after 10 refinements, 120272 Ndof (by using $\eta_{K_l}^{r2}$) after 30 refinements.

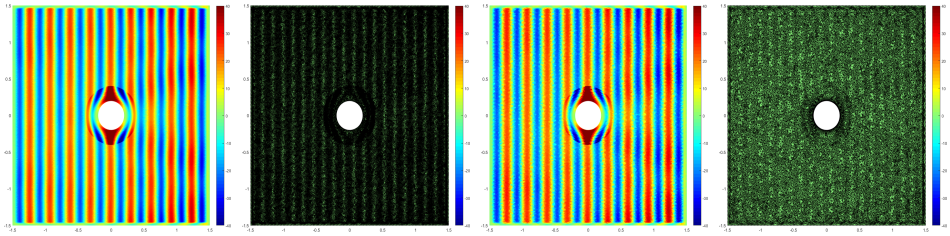

FIGURE 16. Example 4.6: Snapshots of numerical solution and adaptive meshes for the real values of E_2. First two columns: 291690 Ndof (by using $\eta_{K_l}^{r1}$) after 10 refinements; The last two columns: 78497 Ndof (by using $\eta_{K_l}^{r2}$) after 34 refinements.

Remark 4. The relationship between the direction of wave source and the position of metamaterial plays a very important role in the actual simulation.

5. **Conclusions.** In this paper, we used adaptive edge element method for the time-harmonic Maxwell's equation, which was not only based on the residual type *a-posteriori* estimation, but also based on the recovery type. And we presented the numerical examples to illustrate the reliability and efficiency of the proposed *a-posteriori* error estimations. By adding the different wave source terms, the results were similar to those obtained by the time domain Maxwell's equations simulations [18, 36]. Through the results of these examples, it can see that the recovery type *a-posteriori* error indicator deserves to be considered and recommended on the each sub-area.

Acknowledgments. Wang's research was supported by Hunan Provincial Innovation Foundation for Postgraduate(CX20190464). Yang's research was supported by NSFC Projects 11771371, Key Project of Hunan Education Department, China 18A056 and Project of Scientific Research Fund of Hunan Provincial Science and Technology Department(No: 2018WK4006). Huang's reserach was supported by NSFC Projects 11971410.

REFERENCES

[1] K. Ando, H. Kang and H. Liu, Plasmon resonance with finite frequencies: A validation of the quasi-static approximation for diametrically small inclusions, *SIAM J. Appl. Math.*, **76** (2016), 731–749.

[2] G. Bao, H. Liu and J. Zou, Nearly cloaking the full Maxwell equations: Cloaking active contents with general conducting layers, *J. Math. Pures. Appl. (9)*, **101** (2014), 716–733.

[3] J.-P. Berenger, A perfectly matched layer for the absorption of electromagnetic waves, *J. Comput. Phys.*, **114** (1994), 185–200.

[4] E. Blåsten, H. Li, H. Liu and Y. Wang, Localization and geometrization in plasmon resonances and geometric structures of Neumann-Poincaré eigenfunctions, *ESAIM Math. Model. Numer. Anal.*, **54** (2020), 957–976.

[5] J. H. Bramble and J. E. Pasciak, Analysis of a Cartesian PML approximation to the three dimensional electromagnetic wave scattering problem, *Int. J. Numer. Anal. Model.*, **9** (2012), 543–561.

[6] S. C. Brenner, J. Gedicke and L.-Y. Sung, An adaptive P_1 finite element method for two-dimensional Maxwell's equations, *J. Sci. Comput.*, **55** (2013), 738–754.

[7] S. C. Brenner, J. Gedicke and L.-Y. Sung, An adaptive P_1 finite element method for two-dimensional transverse magnetic time harmonic Maxwell's equations with general material properties and general boundary conditions, *J. Sci. Comput.*, **68** (2016), 848–863.

[8] Z. Cai and S. Cao, A recovery-based a posteriori error estimator for $H(\mathbf{curl})$ interface problems, *Comput. Methods. Appl. Mech. Engrg.*, **296** (2015), 169–195.

[9] Z. Cai and S. Zhang, Recovery-based error estimators for interface problems: Mixed and nonconforming finite elements, *SIAM J. Numer. Anal.*, **48** (2010), 30–52.

[10] Z. Cai and S. Zhang, Flux recovery and a posteriori error estimators: Conforming elements for scalar elliptic equations, *SIAM J. Numer. Anal.*, **48** (2010), 578–602.

[11] J. Cui, Multigrid methods for two-dimensional Maxwell's equations on graded meshes, *J. Comput. Appl. Math.*, **255** (2014), 231–247.

[12] Y. Deng, H. Liu and G. Uhlmann, Full and partial cloaking in electromagnetic scattering, *Arch. Ration. Mech. Anal.*, **223** (2017), 265–299.

[13] W. Dörfler, A convergent adaptive algorithm for Poisson's equation, *SIAM J. Numer. Anal.*, **33** (1996), 1106–1124.

[14] Y. Hao and R. Mittra, FDTD modeling of metamaterials: Theory and applications, *Artech. House.*, (2008).

[15] B. He, W. Yang and H. Wang, Convergence analysis of adaptive edge finite element method for variable coefficient time-harmonic Maxwell's equations, *J. Comput. Appl. Math.*, **376** (2020), 16pp.

[16] Y. Huang, J. Li and C. Wu, The averaging technique for superconvergence: Verification and application of 2D edge elements to Maxwell's equations in metamaterials, *Comput. Methods Appl. Mech. Engrg.*, **255** (2013), 121–132.

[17] Y. Huang, J. Li and W. Yang, Interior penalty DG methods for Maxwell's equations in dispersive media, *J. Comput. Phys.*, **230** (2011), 4559–4570.
[18] Y. Huang, J. Li and W. Yang, Modeling backward wave propagation in metamaterials by the finite element time-domain method, *SIAM J. Sci. Comput.*, **35** (2013), B248–B274.
[19] Y. Huang and N. Yi, The superconvergent cluster recovery method, *J. Sci. Comput.*, **44** (2010), 301–322.
[20] H. Li, J. Li and H. Liu, On quasi-static cloaking due to anomalous localized resonance in $\mathbb{R}^3$, *SIAM J. Appl. Math.*, **75** (2015), 1245–1260.
[21] H. Li, S. Li, H. Liu and X. Wang, Analysis of electromagnetic scattering from plasmonic inclusions beyond the quasi-static approximation and applications, *ESAIM Math. Model. Numer. Anal.*, **53** (2019), 1351–1371.
[22] J. Li and J. S. Hesthaven, Analysis and application of the nodal discontinuous Galerkin method for wave propagation in metamaterials, *J. Comput. Phys.*, **258** (2014), 915–930.
[23] J. Li, Y. Huang and W. Yang, An adaptive edge finite element method for electromagnetic cloaking simulation, *J. Comput. Phys.*, **249** (2013), 216–232.
[24] H. Liu, Virtual reshaping and invisibility in obstacle scattering, *Inverse Problems*, **25** (2009), 16pp.
[25] P. Monk, *Finite Element Methods for Maxwell's Equations*, Oxford University Press, New York, 2003.
[26] A. Naga and Z. Zhang, A posteriori error estimates based on the polynomial preserving recovery, *SIAM J. Numer. Anal.*, **42** (2004), 1780–1800.
[27] N. C. Nguyen, J. Peraire and B. Cockburn, Hybridizable discontinuous Galerkin methods for the time-harmonic Maxwell's equations, *J. Comput. Phys.*, **230** (2011), 7151–7175.
[28] J. B. Pendry, D. Schurig and D. R. Smith, Controlling electromagnetic fields, *Science*, **312** (2006), 1780–1782.
[29] N. A. Pierce and M. B. Giles, Adjoint recovery of superconvergent functionals from PDE approximations, *SIAM. Rev.*, **42** (2000), 247–264.
[30] A. Taflove and S. C. Hagness, *Computational Electrodynamics: The Finite-Difference Time-Domain Method*, Artech House, Inc., Boston, MA, 2000.
[31] H. Wang, W. Yang and Y. Huang, Adaptive finite element method for the sound wave problems in two kinds of media, *Comput. Math. Appl.*, **79** (2020), 789–801.
[32] D. H. Werner and D.-H. Kwon, *Transformation Electromagnetics and Metamaterials. Fundamental Principles and Applications*, Springer-Verlag, London, 2014.
[33] W. Yang, Y. Huang and J. Li, Developing a time-domain finite element method for the Lorentz metamaterial model and applications, *J. Sci. Comput.*, **68** (2016), 438–463.
[34] W. Yang, J. Li and Y. Huang, Modeling and analysis of the optical black hole in metamaterials by the finite element time-domain method, *Comput. Methods Appl. Mech. Engrg.*, **304** (2016), 501–520.
[35] W. Yang, J. Li and Y. Huang, Mathematical analysis and finite element time domain simulation of arbitrary star-shaped electromagnetic cloaks, *SIAM J. Numer. Anal.*, **56** (2018), 136–159.
[36] W. Yang, J. Li, Y. Huang and B. He, Developing finite element methods for simulating transformation optics devices with metamaterials, *Commun. Comput. Phys.*, **25** (2019), 135–154.
[37] O. C. Zienkiewicz and J. Z. Zhu, The superconvergence patch recovery (SPR) and adaptive finite element refinement, *Comput. Methods. Appl. Mech. Engrg.*, **101** (1992), 207–224.

Received February 2020; revised April 2020.

E-mail address: wanghao106031@126.com
E-mail address: yangweixtu@126.com
E-mail address: huangyq@xtu.edu.cn